Applied Physics Laboratory

University of Washington

1013 NE 40th Street
Box 355640
Seattle, WA 98105-6698

206-543-1300
FAX 206-543-6785
www.apl.washington.edu

27 March 2014

To: Dr. Robert Headrick, Code 322
         Office of Naval Research
         875 N. Randolph St.
         Arlington, VA 22203-1995

From: James A. Mercer
         Andrew W. White

Subj: ONR Grant # N00014-08-1-0200, "Deep-Water Acoustics [Special Graduate Traineeship Award
         in Ocean Acoustics]"

Encl: (1) Andrew W. White, Rex K. Andrew, James A. Mercer, Peter F. Worcester, Matthew A. Dzieciuch,
         and John A. Colosi, "Wavefront intensity statistics for 284-Hz broadband transmissions to 107-km
         range in the Philippine Sea: observations and modeling", J. Acoust. Soc. Am., 134(4), Pt. 2,
         October 2013, with attached SF298.
         (2) List of all presentations and publications completed over the life of the subject grant.

The attached (Encl 1) constitutes the final technical report for grant # N00014-08-1-0200. The report also contains
documentation (Encl 2) for all other publications and presentations produced during the life of the subject grant.

In addition, Dr. White's dissertation "Underwater Propagation in the Philippine Sea: Intensity Fluctuations" was
submitted to you via the AMRDEC SAFE website on 4 March 2014.

These three components constitute the final deliverables for the subject grant.

cc: Administrative Grants Officer, ONRRO Seattle
         Grant & Contract Administrator, APL-UW
         Office of Sponsored Programs, UW
         Naval Research Lab, Code 5596
         Defense Technical Information Center

CrossMark
click for updates

Wavefront intensity statistics for 284-Hz broadband transmissions to 107-km range in the Philippine Sea: Observations and modeling

Andrew W. White[a)]
Department of Earth and Space Sciences, University of Washington, Seattle, Washington 98105

Rex K. Andrew and James A. Mercer
Applied Physics Laboratory, University of Washington, Seattle, Washington 98105

Peter F. Worcester and Matthew A. Dzieciuch
Scripps Institution of Oceanography, University of California at San Diego, La Jolla, California 92093

John A. Colosi
Department of Oceanography, Naval Postgraduate School, Monterey, California 93943

In the spring of 2009, broadband transmissions from a ship-suspended source with a 284-Hz center frequency were received on a moored and navigated vertical array of hydrophones over a range of 107 km in the Philippine Sea. During a 60-h period over 19 000 transmissions were carried out. The observed wavefront arrival structure reveals four distinct purely refracted acoustic paths: One with a single upper turning point near 80 m depth, two with a pair of upper turning points at a depth of roughly 300 m, and one with three upper turning points at 420 m. Individual path intensity, defined as the absolute square of the center frequency Fourier component for that arrival, was estimated over the 60-h duration and used to compute scintillation index and log-intensity variance. Monte Carlo parabolic equation simulations using internal-wave induced sound speed perturbations obeying the Garrett–Munk internal-wave energy spectrum were in agreement with measured data for the three deeper-turning paths but differed by as much as a factor of four for the near surface-interacting path. © *2013 Acoustical Society of America.*
[http://dx.doi.org/10.1121/1.4818886]

I. INTRODUCTION

In the geometrical optics description of sound propagation in an ocean with a deep sound channel, most of the contribution to acoustic scattering is thought to occur at upper turning points (UTP) (Flatté *et al.*, 1979). Here, the acoustic path is horizontal, and is aligned with the largest correlation-length scales in the inhomogeneity of sound speed (which is greatest in the upper ocean), maximizing their effect. However, it is less well-known how intensity fluctuations develop with the number of turning points or depend on turning-point depth. Also not well-known is at what ranges, and to what extent, penetration of acoustic energy into geometric shadow zones ["shadow-zone arrivals" (Dushaw *et al.*, 1999; van Uffelen, 2009; van Uffelen *et al.*, 2010)] should be expected for a given experimental geometry; e.g., is the effect cumulative? Acoustic frequency should determine, in general, the relative importance of spatial scales that influence intensity fluctuations, thus potentially emphasizing different sources of sound-speed variability in the ocean. Whether all of these answers depend on the character of the local oceanography may also be an important consideration. At long range, acoustic paths pass through the upper ocean many times before reaching a receiving hydrophone; the physical mechanisms responsible for particular features of acoustic intensity fluctuations may be obscured by multiple scattering events.

A common measure of acoustic scattering is the fluctuation of intensity. Intensity fluctuations have been measured in many previous short-range experiments (e.g., Ewart, 1976; Worcester, 1979; Ewart and Reynolds, 1984; Reynolds *et al.*, 1985), although most short-range experiments involved transmission of frequencies in the kHz range. An exception was the ATOC Engineering Test (AET) described in Worcester *et al.* (1999). AET was one of only two short-range (<500 km) low-frequency (<1 kHz) scattering experiments that have been conducted to date [the other being some of the stations in the Long-range Ocean Acoustic Propagation Experiment (LOAPEX) (Mercer *et al.*, 2009)]. One portion of AET involved transmissions at an acoustic frequency of 75 Hz over 87 km paths in the Eastern North Pacific Ocean with only one or two UTP. In an analysis of the AET measurements, the scintillation index was reported to be an order of magnitude larger for the path with two UTP than for a path that had only one (Colosi *et al.*, 2009).

In May of 2009, a pilot study/engineering test (PhilSea09) was conducted in the Philippine Sea. For an overview of efforts conducted in the Philippine Sea during 2009-2011 by the North Pacific Acoustic Laboratory (NPAL) (Worcester and Spindel, 2005), see Worcester *et al.*

1

(2012). The experiment design for PhilSea09 was meant to provide high evolution-time resolution time series of low-frequency broadband transmissions over a short range, involving paths with one or a few interactions with the upper ocean. Phase-coded m-sequences (Birdsall and Metzger, 1986; Birdsall, 1995) with a 284 Hz center frequency were transmitted from an acoustic projector that was suspended from the R/V *Melville* to a depth near the local sound-speed minimum of the deep sound channel. The transmissions were made at a nominal range of 107 km from a distributed vertical line-array of hydrophones (DVLA) (Worcester *et al.*, 2009) that was deployed as a part of the broader, multi-institution experimental efforts. These measurements are unique in that they provide an unprecedented evolution-time resolution, making it possible to see intensity evolve at 7.2-s intervals. Two of the paths in PhilSea09 were quite similar to the paths in AET. Unlike the AET experiment, transmissions were made nearly continuously (except for some necessary gaps in time, which will be discussed later) and were made in the oceanographically highly energetic Philippine Sea—while AET (along with many other low-frequency experiments) was undertaken in the Eastern North Pacific Ocean.

Maps of the variance of sea-surface height for time scales of 65 days to 220 days (Kobashi and Kawamura, 2001) suggest that mesoscale activity in the Philippine Sea should be far more prevalent than in the comparatively quiescent propagation environment of the Eastern North Pacific Ocean. This difference might lead one to expect that range-dependence of the sound-speed field would be a necessary feature of successful ocean models used for acoustic propagation studies in the region. Alford *et al.* (2011) measured baroclinic energy, energy fluxes, and turbulent dissipation in the Luzon Strait and found these quantities to be "among the strongest ever measured"; PhilSea09 was conducted approximately 510 km to the East of the Luzon Strait, which would lead one to expect some deterministic temporal dependence of the sound-speed field on tidal time scales.

The purpose of this work is twofold: First, we report measurements of fluctuations in acoustic intensity made in 2009 in the Philippine Sea, including experimental goals and methods; second, we compare these measurements to Monte Carlo parabolic equation (MCPE) simulations. Time series of acoustic intensity are analyzed to get estimates of measures of fluctuations; these estimates are then compared to a MCPE model with random perturbations of a range-independent background sound speed.

MCPE is a method of modeling acoustic fluctuations that are induced by variability in the ocean. MCPE simulations have been used by Colosi *et al.* (1994), Wolfson and Spiesberger (1999), Xu (2007), and van Uffelen (2009) among others. Ocean variability as it pertains to ocean acoustics includes, but is not limited to, displacements due to ocean internal tides, vertical displacements by a background of diffuse internal waves, mesoscale eddy propagation, and spice (buoyancy-compensated water masses with sound speed that is different than surrounding water masses). This particular implementation of the MCPE method includes only diffuse internal waves. The parabolic equation contains the relevant physics for propagation; the MCPE method provides an

evaluation of the simulated propagation environment, which is composed of a background sound-speed plus perturbations. The perturbations are modeled as being due to ocean internal waves as described by the Garrett–Munk (GM) spectrum (Munk, 1981). We do not assert that the GM spectrum is necessarily the optimal model for diffuse internal waves (various corrections or alternative descriptions have been proposed, e.g., Levine, 2002; Pinkel, 1984) but only that it is a reasonable starting-point in attempts to understand acoustic fluctuations. The goal for the comparison to MCPE simulations is to test whether the non-diffuse-internal-wave aspects of the local oceanography cause overwhelming differences in the character of intensity fluctuations, thus precluding inter-regional comparison to experiments conducted in the Eastern North Pacific Ocean—where predictions of MCPE using a GM internal-wave description have largely been successful. As an example, Xu (2007) conducted broadband simulations that predict the order-of-magnitude difference in scintillation index for the two paths in the AET experiment.

The organization of this paper is as follows: Sec. II gives a description of the experimental methods along with the acoustic and environmental observations made. Section III examines the MCPE model. This section contains an analysis of temperature, salinity, and pressure measurements collected by instruments on the DVLA for the purpose of adjusting the GM model displacements to a value appropriate for the region. MCPE results for the adjusted model are presented along with the measured acoustic fluctuations in Sec. IV. Section V includes a discussion of the comparison, and Sec. VI provides conclusions and a direction for further study. The appendix describes the convergence tests that determined the maximum internal-wave mode number to be included in the ocean model and the appropriate PE range-step.

II. EXPERIMENT

A. Overview

A map of the region of the experiment, including the location of the DVLA and the R/V *Melville*'s position during acoustic transmissions appears in Fig. 1. The location of the ship during acoustic transmissions was designated "SS107" due to its nominal range of 107 km from the DVLA. The ship's position was determined by a C-Nav GPS receiver, which was described previously in Mercer *et al.* (2009). The C-Nav's antenna was located on the R/V *Melville*'s A-frame, directly above the deployment sheave used to support the acoustic projector, which was suspended over the stern.

The projector was lowered to a depth of 1000 m. The depth of the sound speed minimum was later determined from smoothed, averaged conductivity, temperature, depth (CTD) cast data to be 1040 m. Measurements taken from a pressure gauge attached to the projector were used to track its depth during transmissions. These measurements, along with other diagnostic measurements, such as the temperature of the power transformer in the transmitter package, and the transmitted acoustic level, were sent up the suspending cable through an optical fiber. At SS107, two acoustic transponders were deployed along the geodesic connecting the projector and the DVLA for the purpose of tracking the
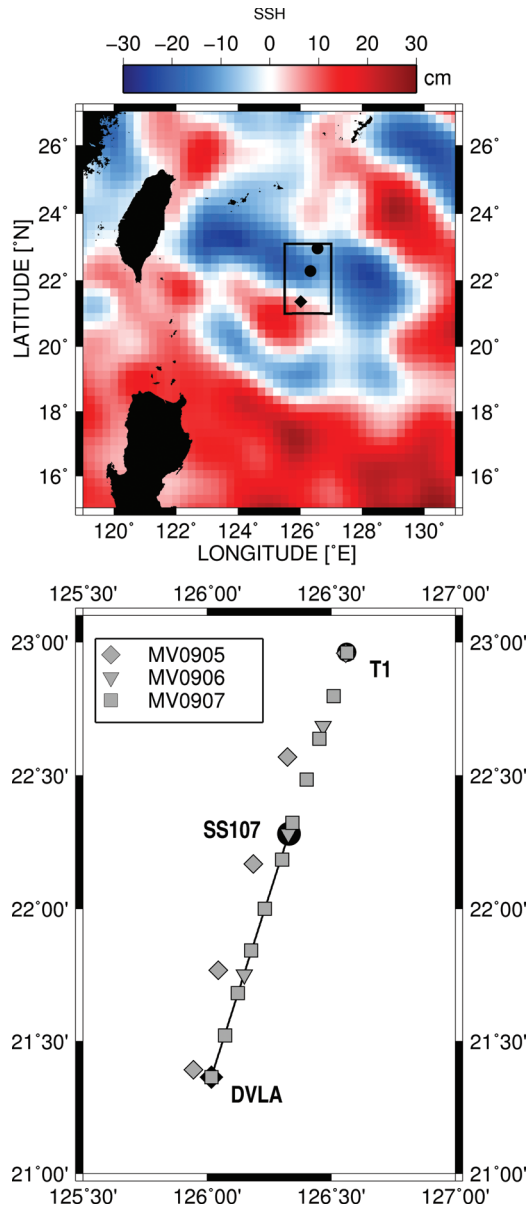
White *et al.*: Intensity stats 284-Hz transmission to 107 km

FIG. 1. Experimental plan for the PhilSea09 experiment. The top panel shows the region, including the islands of Taiwan and Luzon at 121° E Longitude, 24° and 17° N Latitude, respectively. The color scale shows the sea-surface height for YD 119 of 2009 from the AVISO (Aviso and support from Cnes, 2012) database. The bottom panel shows the region bounded by the rectangle in the top panel. Sets MV0905, MV0906, and MV0907 denote CTD casts made on three consecutive 2009 cruises. The surveyed locations of the transmitter at station SS107 and the DVLA were 22.282 500° N, 126.329 445° E and 21.364 963° N, 126.017 090° E, respectively. The label "T1" refers to an acoustic transceiver mooring also deployed as part of PhilSea09, but is only shown here for context and will not be discussed in this work.

projector's position during transmissions. An acoustic pinger was located on the transmitter package and interrogated the bottom-deployed transponders, forming a long-baseline transponder net.

The over-the-side transmitter package (Andrew, 2009) was assembled and deployed over the stern of the R/V *Melville* by the Applied Physics Laboratory at the University of Washington (APL/UW). The package consisted of an experimental double-ported doubly resonant electro-acoustic transducer, designated MP200/TR1446, designed by

ImageAcoustics Inc. and manufactured by Massa Products, Inc., a matching auto-transformer/tuner manufactured by Coiltron, Inc., a tracking pinger, auxiliary sensors, and battery power for the sensors.

The MP200/TR1446 was operated between two resonances, both quite sharp at about 210 and 320 Hz, in an attempt to provide a "broadband" device. A model of the complete system transfer function is shown in Fig. 2. It was desired to attempt to utilize the full broadband bandwidth of the device, and therefore a $Q = 2$ drive signal was designed
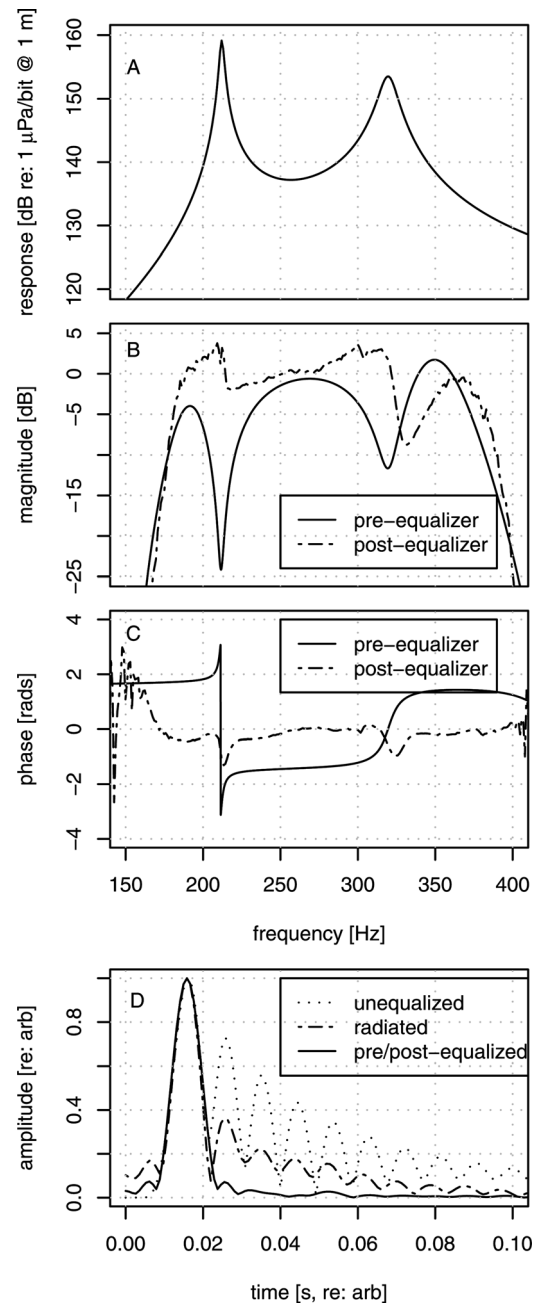

FIG. 2. Transmission signal design, PhilSea09. (A) Theoretical system transfer function into the water computed from equivalent circuit model. (B) Magnitude of the pre- and post-equalizer filters. (C) Phase of the pre-and post-equalizer filters. (D) Pulse-compressed m-sequences without any equal-ization, with pre-equalization after passing through the system (chiefly the MP200/TR1446 transducer) into the water ("radiated"), and receiver wave-form after post-equalization.

3

that had a 1023-bit m-sequence (Munk *et al.*, 1995), a carrier frequency of 284 Hz, and two cycles of the carrier for each bit of the sequence. This signal had an approximate bandwidth of 142 Hz, from about 212 to 356 Hz, a band that roughly incorporates both resonant peaks. Because the system response was far from flat over this band, an equalization filter was designed to compensate for the dual-peaked response. This filter was applied to the drive signal prior to transmission, and hence is called the "pre-equalizer." The transfer function of the pre-equalizer is shown in Fig. 2. Without equalization, the system distortion introduced significant "ringing" after the pulse-compressed pulse of the m-sequence. The theoretical performance of the pre-equalizer eliminated the ringing in pre-cruise models.

After the cruise, inspection of the waveforms received on a package monitor hydrophone and on the DVLA hydrophones indicated that the pre-equalizer was not accurately compensating for the system transfer function. Therefore a further "post-equalizer" filter was designed, based on Wiener filter theory, and applied on the received data. The response of the post-equalizer is also shown in Fig. 2. The final result on pulse compression using both pre- and post-equalization is shown in the bottom panel of Fig. 2: The post-equalizer completed the task of adjusting the received signal Fourier content (i.e., phase and magnitude) into a reasonable facsimile of the Fourier characteristics of an m-sequence with a 130 Hz bandwidth and pulse resolution of 7.7 ms. The RMS source level, measured in the water with the transmitter package monitor hydrophone, was roughly 183 dB re 1 μPa @ 1 m. The vertical beam-width of the MP200/TR1446 was 120°; the transducer is omni-directional in azimuth.

Acoustic signals were transmitted from SS107 for approximately 60 h, compared to the local inertial period of 32 h. Thus our observations include nearly two periods of the slowest internal waves (which, admittedly is not enough time to study the statistics of acoustic fluctuations due to these slowest waves), but 90 cycles of waves at 6 cycles per h (this was the surface-extrapolated buoyancy frequency in the region of the experiment). Our observations are not of sufficient duration to study the statistics of slower ocean processes, such as mesoscale eddies.

The acoustic signals were m-sequences with a duration of 7.2 s and were transmitted nearly continuously from SS107. The planned transmission schedule included gaps at the change of each hour to ensure that acoustic tracking of the DVLA's position would not be affected. Further gaps in transmission were necessary to prevent overheating of the power amplifier. These data were post-equalized and then pulse-compressed in the standard way (Birdsall and Metzger, 1986; Birdsall, 1995). Some data were contaminated due to power amplifier glitches or due to sonar signals of unknown origin; these data were also removed.

The DVLA was located at 21.364 963° N, 126.017 090° E and is described in further detail in Worcester *et al.* (2012); we provide here only the details pertinent to our analysis. The DVLA was composed of both upper and lower sub-arrays, each consisting of 30 hydrophones. The upper sub-array spanned the deep sound channel axis, or sound speed minimum. This upper sub-array had hydrophones at

depths of 651 and 725 m, and then every 25 m from 800 to 1400 m, followed by hydrophones at 1475, 1550, and 1625 m. Receptions made on the lower sub-array are not discussed in this paper. The hydrophones were High Tech, Inc., model HTI-90-U. The sample rate of these hydrophones was set to a nominal value of 1953.125 sample/s, although the clock rate in individual hydrophones varied slightly. This clock-rate error was determined for individual hydrophones and an appropriate correction was applied.

Significant "blow-downs" of the DVLA occurred during the month of its deployment, presumably as a result of the strong local internal tides. These low-velocity blow-downs resulted in changes in hydrophone position of up to 90 m in the vertical and up to a few hundred meters in the horizontal. Intensities computed by ray-tracing [with the RAY program (Bowlin *et al.*, 1992)] indicated that the effects of changes in hydrophone position were not large enough to be considered significant. The ship's position was maintained by a dynamic positioning system, but ship heave due to wave motion and currents resulted in motion of the acoustic projector. The effects of projector motion on intensity (a Doppler shift in the signal, which reduces the gain achieved by pulse-compression) were also found not to be significant.

B. Acoustic data

The RAY program, with the background sound speed profile $\bar{c}(z)$ as input, was used to model the acoustic paths studied here; $\bar{c}(z)$ and several representative paths are shown in Fig. 3. The ID nomenclature used in the figure is a concise way of describing key features of a given acoustic path
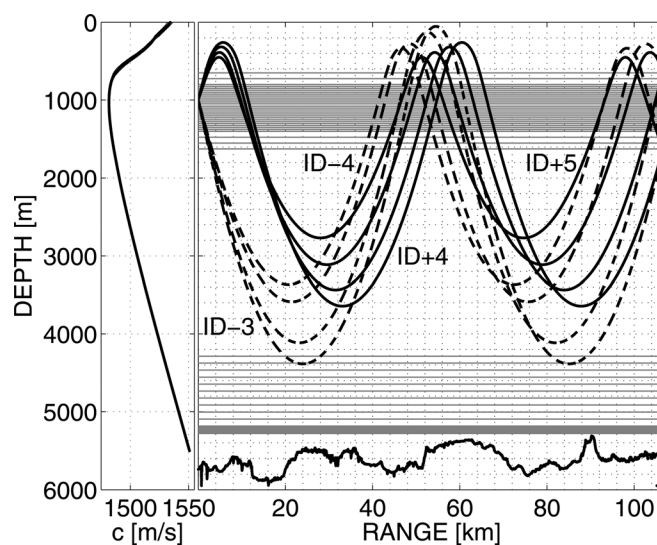

FIG. 3. The vertical sound-speed profile used in this work is shown at left; at the right are the typical eigenrays studied. The gray horizontal lines represent the depths of hydrophones on the upper and lower sub-arrays on the DVLA, and the solid gray band near the bottom is a closely spaced (5 m) group of hydrophones. We study receptions on all 30 hydrophones of the upper subarray for the paths marked "ID-3," "D+4," "ID-4," and "ID+5." Only eigenrays reaching the shallowest and deepest hydrophones on the upper sub-array (651 and 1625 m depth) are shown. Paths leaving the source at an upward angle are shown with solid curves; paths leaving the source at a downward angle are shown with dashed curves. The solid black curve at the bottom of the figure is the bathymetry that was measured along the propagation path with the R/V *Melville's* multi-beam sonar.

White *et al.*: Intensity stats 284-Hz transmission to 107 km

4

between a transmitter and receiver. The $+/-$ sign refers to the sign of the angle made between the associated acoustic energy leaving the projector and the horizontal, while the number that follows refers to the number of upper and lower turning points for that path between the transmitter and receiver. The paths shown reaching the upper sub-array of the DVLA are refracted-only in the sound-speed profile shown in the figure. There is a surface-bounce path that arrives 40 ms after the first arrival (ID-3) at the upper sub-array, but we neglect it here as the pulse width of the processed receptions was 7.7 ms, so that we may window out this surface-bounce path in time.

Throughout this paper, we will refer to transmissions received on the upper sub-array at all receiver depths; in particular, we will study paths ID-3, ID+4, ID-4, and ID+5. These paths are separable in time except that for a few depths near the center of the sub-array paths ID+4 and ID-4 may not be separated from each other, and at the bottom of the sub-array path ID+5 may not be separated from later arrivals. Upper turning depths for the four paths are given in Table I.

Each arrival is tracked using the acoustic transponder navigation solution for the array position. We find the peak of the arrival envelope, window data in a 10 ms window and take the Fourier-transform; the absolute square of the 284 Hz component is computed as the single-frequency intensity.

An example set of 60 h time series of acoustic log-intensity for the four paths that was recorded on the 900 m depth hydrophone is shown in Fig. 4. These are characteristic of the records for the great majority of hydrophones and represent the first-order acoustic fluctuations modeled in this paper. An additional time series of intensity for ID-3 from a hydrophone at 1550 m depth is also shown in the figure. Readily apparent in the 1550 m ID-3 time series are long-period deep fades. Similar fading does not appear in the records for ID+4, ID-4, and ID+5, nor is there any other obvious feature in these intensity records at times when fading is observed in ID-3. The fading in path ID-3 is most apparent at depths 1150 m and deeper and becomes more pronounced with increasing depth.

C. Environmental data

A total of 81 expendable bathythermograph (XBT) casts were made along the geodesic connecting the DVLA and SS107 positions. Mixed layer depths as deep as 80 m were measured to the northeast of SS107 in these casts; also apparent was strong range-dependence in the upper ocean. Satellite-based measurements of sea-surface height from the AVISO (Aviso and support from Cnes, 2012) database
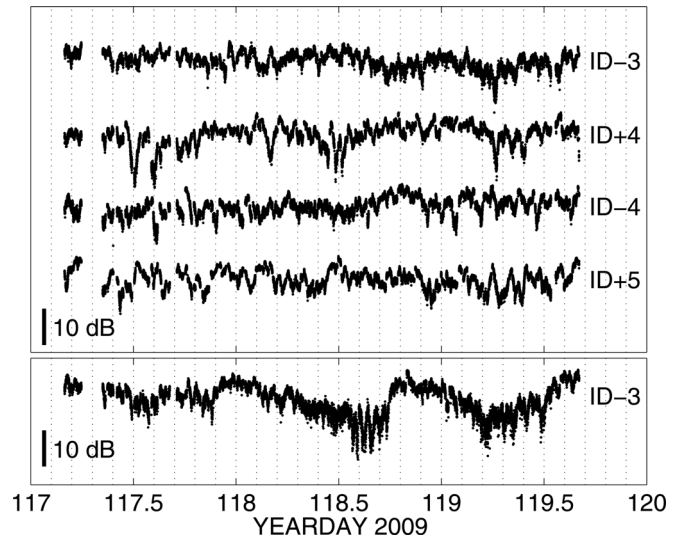

FIG. 4. The top panel shows as an example time series of $10\log_{10}(I/\langle I\rangle)$, recorded on the 900 m hydrophone, for paths ID-3, ID+4, ID-4, and ID+5. The bottom panel shows ID-3 for the 1550 m hydrophone—an example of the deep fades (at YD 118.5 and 119.25) observed on the deeper phones of the shallow array. A bar representing the scale appears in both panels to the left of the label "10 dB".

exhibit sea surface height anomalies with a sign consistent with the horizontal temperature variation measured by the XBT casts (shown in Fig. 5). These range-dependent variations could be explained by the presence of eddies.

A total of 21 CTD casts were taken during PhilSea09 over a period of time lasting from April 02 to May 12, along or near the geodesic connecting the DVLA and SS107. The positions of the CTD casts are shown in Fig. 1. Data from 19 of these casts were smoothed and averaged to create the range-independent "background" profiles of sound speed $\bar{c}(z)$, buoyancy frequency $N(z)$, and the vertical gradient of
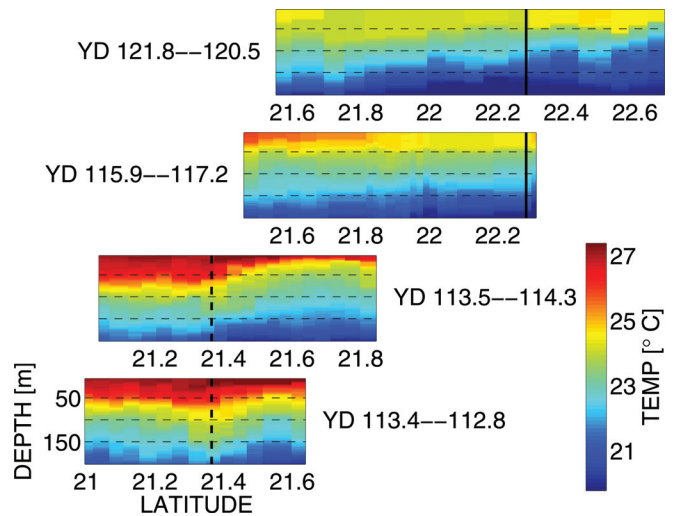

FIG. 5. Shown here are XBT transects of ocean temperature, with latitude increasing from left to right, and time increasing from the bottom to the top of the figure. Note that the time in year days increases from left to right, except in the bottom and top panels as indicated by the labels to the right or left of each panel. Individual casts were made an hour apart in time while the ship was underway. A strong range dependence and some time dependence are evident from the measurements. The vertical dashed and solid lines show the latitudes of the DVLA and SS107, respectively, for reference.

TABLE I. Upper turning point depths and associated receiver depths: For paths ID-3 and ID+4, the shallowest-turning eigenrays reach the deepest receiver of the sub-array; for paths ID-4 and ID+5, the shallowest-turning eigenrays reach the shallowest receiver of the subarray

Path	ID-3	ID+4	ID-4	ID+5
UTP depth (m)	53–126	260–317	276–334	388–451
HYD. depth (m)	1625–651	1625–651	651–1625	651–1625

potential sound speed $d\bar{c}_{Pot.}/dz$ used in MCPE and RAY modeling described in Secs. II B and III.

In addition to profile-type environmental data, time series of temperature, salinity, and pressure were collected throughout April and May with instruments attached to the DVLA (Colosi *et al.*, 2013). Data from these 12 pumped microCAT CTD instruments were analyzed to provide an estimate of GM strength subsequently used in the "adjusted" MCPE model, described in Sec. III B.

III. MODELING

A. Ocean sound speed fluctuations

One parameter that may be adjusted in the GM spectral model of internal waves is the "strength", s_{GM}, which we will describe here as the product

$$s_{GM} = N\langle\zeta^2\rangle = 0.5 \cdot bE_{GM}N_0 b \tag{1}$$

or the variance of the internal wave vertical displacement, ζ, scaled by the buoyancy frequency $N(z)$. In Eq. (1), b is the thermocline depth scale, E_{GM} is the reference internal-wave energy level, and N_0 is the reference buoyancy frequency. Although ζ and N are functions of depth, their product, s_{GM}, is a constant, independent of depth. In the approach taken in this paper, we adjust the quantity s_{GM} in our simulated oceans to match the value we will here estimate from environmental observations.

After summation over the vertical internal-wave modes, the GM vertical-displacement spectrum $F_{\zeta\zeta}$ (scaled by N) is given by the equation

$$NF_{\zeta\zeta}(\omega) = \frac{2bE_{GM}N_0 b\omega_i\sqrt{\omega^2-\omega_i^2}}{\omega^3\pi}, \tag{2}$$

where ω is frequency, and ω_i is the inertial frequency. Ocean internal waves exist at temporal frequencies between the inertial frequency and the local buoyancy frequency.

We seek to make an estimate of the scaled variance of displacement $N\langle\zeta^2\rangle$, which is equal to the integral over frequency of Eq. (2). The best source of information about temporal variability of the propagation environment was the collection of microCAT CTDs deployed on the DVLA. Time series of displacement may be computed from the temperature, salinity, and pressure records obtained by these instruments and then examined in various ways to get estimates of the GM strength for the Philippine Sea. We express this strength as the ratio $\hat{r}$ of the measured strength $\hat{s}$ to the standard GM strength

$$\hat{r} = \frac{\hat{s}}{s_{GM}} = \frac{\widehat{N\langle\zeta^2\rangle}}{N\langle\zeta^2\rangle}. \tag{3}$$

One approach would be to high-pass filter the time series of displacement above the inertial frequency and then calculate the variance of the resultant time series, assuming the spectrum falls rapidly—such that any part of the spectrum above the local buoyancy frequency will provide a negligible contribution. Alternatively, if the tides were well-

known and well-modeled, the time series could be fit with a tidal model, and the fit removed. We choose here to make an estimate of the GM spectral level, $\widehat{F_{\zeta\zeta}(\omega)}$, in the region of the experiment, and integrate it to find an estimate of the strength ratio $\hat{r}$ (recall that multiplication by $N(z)$ makes this ratio depth-independent)

$$\hat{r} = \frac{N\int \widehat{F_{\zeta\zeta}(\omega)}\,d\omega}{N\int F_{\zeta\zeta}(\omega)\,d\omega}. \tag{4}$$

Data from the 12 pumped microCAT CTDs on the DVLA were analyzed as described in the following text to make an estimate of the GM strength parameter. The temperature-salinity-pressure measurements were first converted to sound speed using the TEOS-10 algorithms (TEOS10, 2010) and are shown in Fig. 6. The array blow-downs mentioned earlier introduced fluctuations into the records as a result of the changes in depth of the sensors. The sound speed data were interpolated in depth in an attempt to remove this instrument-caused fluctuation. Several interpolation methods were examined, but the choice of interpolation method did not strongly influence the estimate; for its simplicity, a linear interpolation scheme was chosen. Time series of displacement were computed by the relation

$$\zeta(t;z) = \delta c(t;z)\left(\frac{\partial\bar{c}}{\partial z}\right)_{Pot.}^{-1}. \tag{5}$$

The potential sound-speed gradient is appropriate because we do not want to include the effect of the portion of the gradient that is due to the pressure increase with depth. Spectra were estimated from these time series using the multi-taper approach with a time-bandwidth product of 4. The spectra are shown in Fig. 7.

Various different approaches might be taken to estimate the "background" level of these diffuse internal waves in the region of the experiment. As may be seen in the estimate of
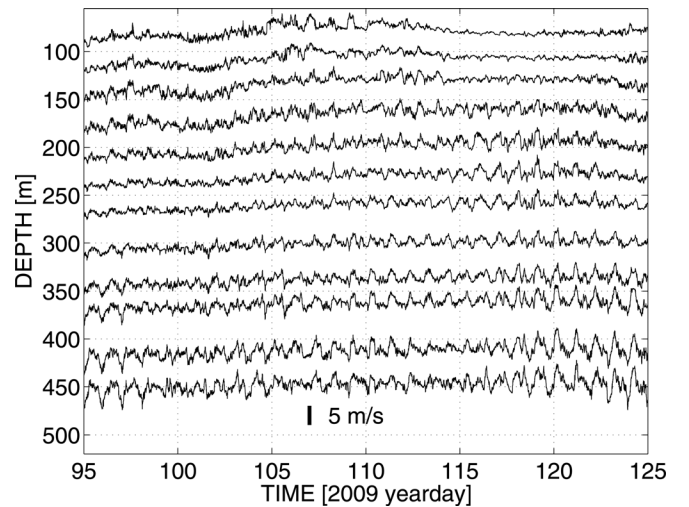

FIG. 6. Time series of sound speed variability computed from CTD measurements made on the DVLA. Each record is offset according to the sensor's mean depth. The vertical bar shows the scale of sound speed fluctuations.
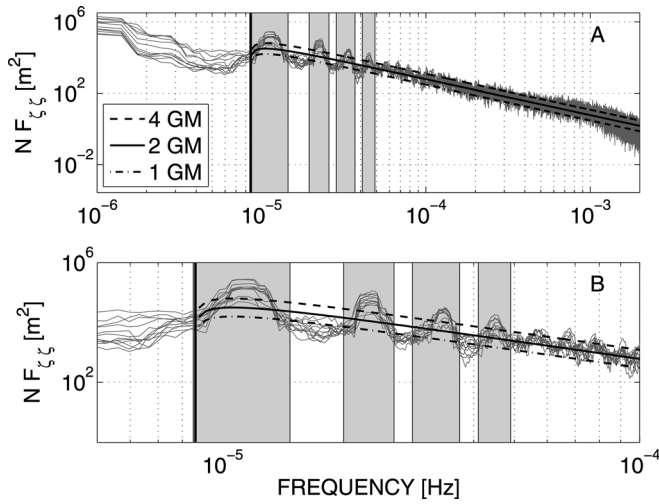
6

FIG. 7. (A) spectra of displacement from the 12 microCAT CTD sensors on the DVLA. The spectra have been scaled by the buoyancy frequency. The thick black vertical line is the inertial frequency. There are four prominent tidal peaks visible in the spectra, known as the K1, M2, K3, M4 tides (Colosi *et al.*, 2013) (in order from left to right) that appear just to the right of the inertial frequency on the plot. The gray shaded regions highlight the frequencies for which these four tidal peaks appear to rise above the background level. Superimposed are the GM spectra for strengths $\hat{r} = 1$, 2, and 4 (appearing from bottom to top) for reference. (B) shows the portion of the spectra near tidal frequencies in greater detail.

the spectrum of sound speed fluctuations shown in Fig. 7, the locally generated internal tides are a prominent source of variability in the Philippine Sea; these tides present a complication in estimating the level of variability due to diffuse internal waves. Ignoring these, the spectrum at higher frequencies appears, visually, to fit reasonably with a GM strength of $\hat{r} = 2$. This should be an useful check against any estimate we might make.

Because it is not clear to what extent the GM spectrum includes contributions from any contaminating local tides, we find it reasonable to make estimates of upper and lower bounds on GM strength for the region of the experiment. In Eq. (4), to calculate an upper bound on the GM strength, we integrate from the inertial to buoyancy frequencies. We consider the quantity

$$\phi(\omega) = \frac{\int_{\omega_i}^{\omega} \widehat{F_{\zeta\zeta}(\omega)}\,\mathrm{d}\omega}{\int_{\omega_i}^{N} \widehat{F_{\zeta\zeta}(\omega)}\,\mathrm{d}\omega}, \qquad (6)$$

where ω_i is the inertial frequency. This is the fraction of the contribution to the integral of $\widehat{F_{\zeta\zeta}}$ as a function of ω. Between 30% and 55% of the variance is due to the K1 tide, 10% to 20% due to the M2, and lesser amounts to the K3 and M4 components (with no easily-discernible trend in depth). In an attempt to calculate a lower bound on GM strength, we want the (local internal, deterministic) tides to be excluded from the variance, and therefore exclude the regions shaded in gray in Fig. 7.

The bounds in frequency of the excluded regions are chosen by eye. The assumption made is that the local tidal energy is defined as energy rising above a background

spectral level due to diffuse internal waves. The extent to which the level between bands is filled in by the energy in the bands is not known. For example, if one were to draw a line through the troughs between bands in Fig. 7, it would not seem to fit the GM model well in terms of its slope, in addition to appearing to be at a lower level than that apparent for higher frequencies. Estimates $\hat{r}$, (averaged in depth) of upper (3.33) and lower (1.6) bounds of GM strength appropriate for the Philippine Sea are given in Fig. 8. The lower estimate of 1.6 seemed to be consistent with the spectral level at higher frequencies and so was chosen as the level to be used in MCPE modeling. This level is in good agreement with the estimate made by Colosi *et al.* (2013), who used a tidal model to estimate and remove tides from the microCAT-derived displacements: Their estimate was a GM strength of 1.4. They conclude that the outlook for modeling the internal tides is unclear; the agreement between our estimates, determined by different approaches, would seem to support the validity of their result.

B. MCPE

The MCPE method is commonly used in the ocean acoustics community to model acoustic signal fluctuations in 2D. The idea is to generate random instances of an inhomogeneous sound-speed field that consists of some range-independent or slowly varying background $\bar{c}(x, z)$ plus perturbations $\delta c(x, z)$ to this background. In this work, we model the background sound speed as range-independent: $\bar{c}(x, z) = \bar{c}(z)$. The sound-speed perturbations are modeled as being solely due to internal waves the statistics of which are consistent with the GM spectrum.

We employ an internal wave simulator that is described in Henyey and Reynolds (2013). The simulator produces vertical "slices" of an internal-wave displacement field, $\zeta(x, z)$, from which perturbations to the background sound speed
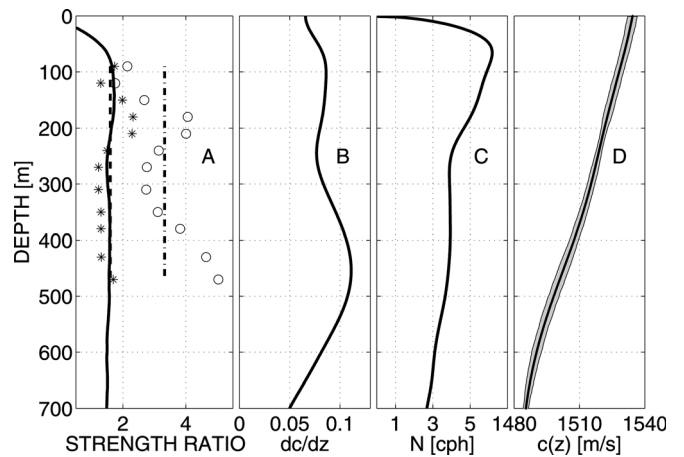

FIG. 8. (A) Estimates of the strength ratio $\hat{r} = \hat{s}/s_{GM}$ made from the individual microCAT sensor time series of displacement. The tides are included in the integral over the spectra shown in Fig. 7 for the estimates shown with a "o" symbol with the mean estimate shown by the dashed-dotted line. The tides are excluded from estimates shown with a "*" with the mean estimate shown by the dashed line. The solid curve shows the strength ratio estimated from 100 simulated oceans. (B) The vertical potential sound speed gradient in ms^{-1} m^{-1}. (C) shows the buoyancy frequency. (D) Smoothed, averaged sound speed, from the 19 CTD casts. The gray region shows 1 std.

7

are calculated. The perturbations are proportional to the vertical gradient in potential sound speed at depth z

$$\delta c(x, z) = \left(\frac{\partial \bar{c}}{\partial z}\right)_{Pot.} \zeta(x, z). \tag{7}$$

An example vertical slice of $\delta c(x, z)$ is shown in Fig. 9.

PE models and associated computer codes that are used for studies of underwater acoustic waves are well-known and plentiful. We chose the Navy Standard Parabolic Equation, or NSPE, for this work—see the appendix for further description. Each perturbed sound speed field is written to an input file for the NSPE code, then broadband propagation through this environment is computed. A time front is produced, from which arrivals are windowed and the single-frequency intensity is computed as was done with the acoustic transmission data.

The source spectrum was modeled as Gaussian, centered at a frequency of $f_{center} = 284$ Hz, and falling to a value of $S(f=f_{center}) * 1/e$ at frequencies of $f_{center} \pm f_{center}/4$. Propagation was calculated at 852 frequencies with a spacing of 1/3 Hz, over the band $f_{center} \pm f_{center}/2$. The frequencies outside the $1/e$ level were included to reduce ringing in the time front.

In the work presented in this report, two types of MCPE simulation are used. In one of the simulations, a time-independent MCPE (which will be referred to as the "TI simulation"), independent random instances of the internal-wave displacement field are computed; in the second simulation, a single random internal-wave displacement field is evolved in time, allowing for time-dependent model-data comparison (the "TD simulation"). The TI simulation consisted of 226 random instances of a 2D (range-depth) slice of perturbed sound-speed, like that shown in Fig. 9. For the TD simulation, the internal-wave displacement field was evolved at a time-step of 240 s for a total of 320 h (ten times the local inertial period, the longest time scale in the GM spectrum), generating a time series composed of a total of 4800 time fronts.

IV. RESULTS

We will consider as measures of the intensity fluctuations the scintillation index (SI) (which is the fourth moment of the acoustic field and the second moment of intensity, normalized by the mean intensity squared)

$$SI = \frac{\langle I^2 \rangle - \langle I \rangle^2}{\langle I \rangle^2}, \tag{8}$$

and the variance of log-intensity, where the log-intensity, ι, is given in dB by $\iota = 10 \log_{10}(I/\langle I \rangle)$, and its variance σ_ι^2

$$\sigma_\iota^2 = \langle \iota^2 \rangle - \langle \iota \rangle^2. \tag{9}$$

Examples of MCPE and observed time fronts are shown in Fig. 10. At some depths, the paths ID+4, ID-4, and ID+5 were not sufficiently separated in time from other paths to allow windowing; these paths are excluded at those depths. The subsets of depths for which it was possible to separate particular arrivals differed slightly between the simulations and measured datasets. It is for this reason that results for histograms, SI, and σ_ι^2 will not be shown at all depths.

Confidence intervals for the TI MCPE simulation are more easily computed than for the experimental data and TD MCPE because all samples in the TI simulation are independent—while the experimental data and the TD MCPE have temporal correlations. For a given hydrophone depth, the set of 226 TI MCPE-derived intensity samples was resampled with replacement to create new sample sets of the same size as the original 1000 times. The SI was computed from each new set and the resulting estimates ordered from smallest to largest. The absolute difference between the 25th ordered estimate(the 2.5% percentile) and the original estimate and the difference between the 975th ordered estimate (the 97.5% percentile) and the original are averaged to give the 95% confidence interval. In the case of the experimental data, the standard error was estimated by block bootstrapping
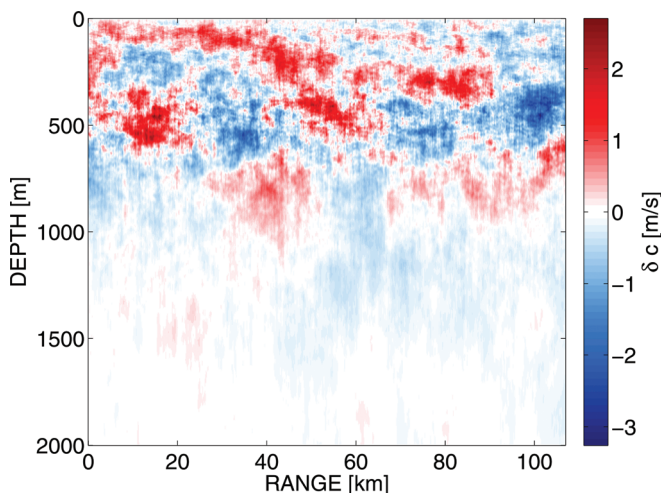

FIG. 9. An example of a $\delta c(x, z)$ range-depth slice from simulation. The full propagation range is shown, but only the upper 2000 m of the slice are shown; fluctuations are much smaller below this depth.
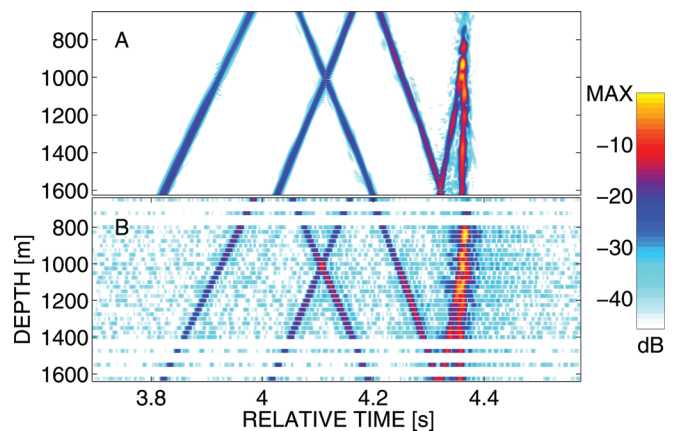

FIG. 10. (A) An example MCPE timefront. (B) An example of a measured time front received on the upper sub-array of the DVLA, after hydrophone clock corrections and post-equalization have been applied. Gaps are due to hydrophone spacing in depth. The first four arrivals on the portion of the array above 1000 m are paths ID-3, ID-4, ID+4, and ID+5, ordered from earlier to later time (the order-of-arrival of paths ID-4 and ID+4 is seen to switch below 1000 m depth). In each panel, the color scale is relative to the maximum intensity shown in the window.

8

(Davison and Hinkley, 1997) with a fixed block size of 400, using the sample variance of the bootstrap sample (Cojbasic and Tomovic, 2007). The standard error was then scaled assuming an asymptotic Gaussian distribution to give the 95% confidence interval. Confidence intervals were computed identically for the variance of log-intensity, σ_l^2.

A comparison of observations and MCPE predictions for the SI and σ_l^2 appears in Fig. 11. The MCPE and data 95% confidence intervals on the SI and σ_l^2 overlap for ID+4, ID-4, and ID+5 at all hydrophone depths. The confidence intervals for data and simulation overlap for ID-3 for depths shallower than 1150 m, although the prediction is consistently slightly smaller than the measured value. The confidence intervals do not overlap for ID-3 for hydrophone depths deeper than 1150 m.

Histograms of observed and modeled $I/\langle I \rangle$ at all hydrophone depths are shown in Fig. 12. Intensities at each depth were sorted into bins with a width of 0.05, and with bin edges ranging from 0 to 3.5. The resulting histogram counts were normalized by the total number of intensities recorded at that depth. For reference, 5% and 1% represent counts of 785 and 157, respectively, for the measured data, and 240 and 48, respectively, for the simulated data.

The distributions of measured intensities exhibit depth-dependence and structure that appear to be consistent across multiple hydrophones. The distribution at several depths around 1300 m appears to be bi-modal for ID+4; the same is true at 725 m for ID-4, and at various depths for ID+5. The mode of the experimentally-measured distributions of ID-3 are shifted increasingly with depth toward low intensities for hydrophones below about 1150 m, and the distribution

FIG. 12. Shown in the left column are normalized histograms of $I/\langle I \rangle$ from the experiment. Shown in the right column are the same from the TD MCPE. Approximately 15 700 samples are included in the histograms at each depth for the measured data, while 4800 samples were included at each depth in the TD MCPE histograms.

widens with depth, with more high intensities on the deeper hydrophones. The low-intensity mode of the ID-3 distribution is consistent with the intensity fading shown in the bottom panel of Fig. 4.

The distributions of the TD MCPE intensities are seen to be uni-modal for all four paths and at all depths for which paths could be separated. The MCPE distribution for ID-3 is noticeably narrower than for the other paths, apparent in the width of the light-blue portion of the histograms—as well as having a mode at a slightly higher intensity. The MCPE histograms appear otherwise to be quite similar to each other over the full range of receiver depths.

V. DISCUSSION

The SI and σ_l^2 predictions for paths ID+4, ID-4, and ID+5 are not different from each other by a statistically significant amount. The predictions for path ID-3 are lower than for the other three paths. The same fluctuation measures of the observed intensities for paths ID+4, ID-4, and ID+5, which had 2, 2, and 3 UTPs, respectively, at depths from 260 to 451 m, were also in agreement with each other. Path ID-3 had one UTP at depths between 53 to 126 m with the shallowest-turning paths reaching the deepest hydrophones on the upper array. At hydrophone depths shallower than 1150 m, the upper bound of the confidence interval on the SI is only slightly greater than the lower bound for paths ID-4 and ID+5 but compares better with path ID+4. For hydrophone depths greater than 1150 m in path ID-3, there is clearly some other modulating process in the intensity record
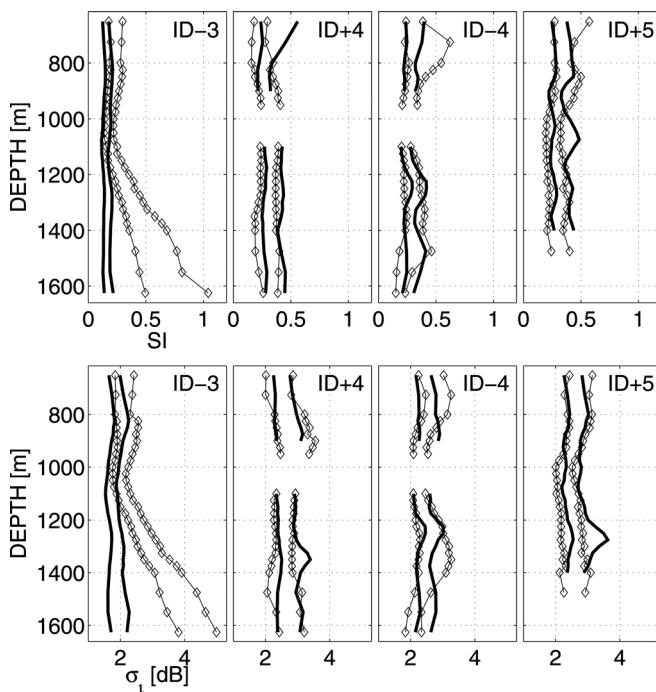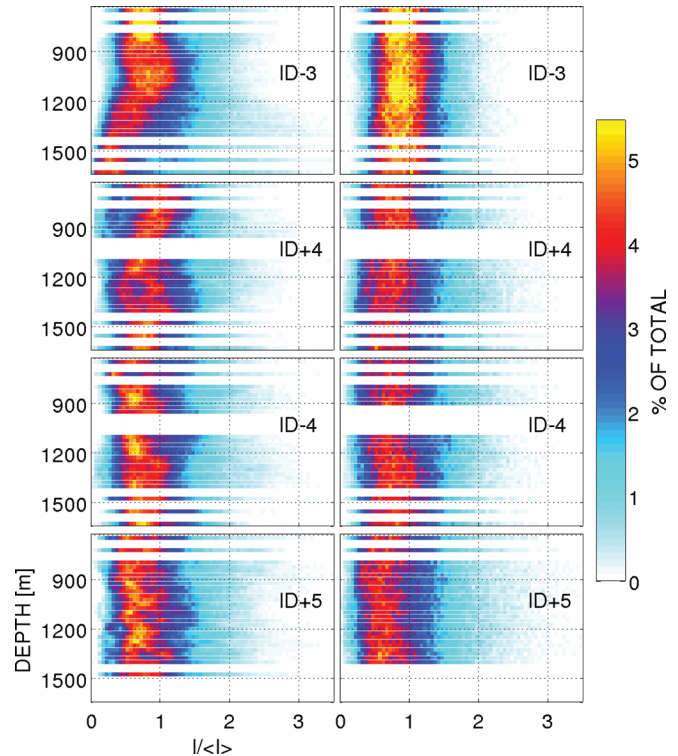

FIG. 11. Top row: Comparison of TI MCPE predictions of SI with measured values. The curves give the 2.5% and 97.5% percentiles—hence the 95% confidence intervals. Bold curves show the MCPE confidence intervals and curves with diamonds show confidence intervals on the measured values. Diamonds indicate the depths at which the measurements were made. The bottom row shows the same for σ_l.

J. Acoust. Soc. Am., Vol. 134, No. 4, Pt. 2, October 2013   White *et al.*: Intensity stats 284-Hz transmission to 107 km   3355

9

that causes it to look qualitatively different than for all other paths. It is not clear whether the number of UTP can be said to affect the strength of the intensity fluctuations in the measured data, given the relatively small differences in SI and σ_l^2 between the various paths—and the possibly significant differences in UTP depth (see Table I).

The MCPE model predicts the SI and σ_l^2 quite well for paths ID+4, ID-4, and ID+5 at hydrophones from 651 to 1625 m depth. The model differs from the observations in that it does not predict these same measures of intensity fluctuations for path ID-3 for hydrophone depths 1150 m and deeper and somewhat underpredicts the variability at the shallower hydrophones for that path.

The TD MCPE distributions of $I/\langle I \rangle$ are similar to those of the measured intensity in the location of the distribution mode for most hydrophone depths, although the measured data exhibit some depth dependence of this mode location. The distributions of the measured data were bi-modal at some depths, while the simulated data had uni-modal distributions. Finally, the high-intensity tails of the measured data extended out further for path ID-3 at depths where fades were observed than for the shallower depths. The length of the measured time series was only about 60 h, while the TD MCPE time series were 320 h in duration; it seems possible that this could be related to the greater depth dependence and structure seen in the distributions of the measured data; i.e., the inclusion of more cycles of the long-period variability could "smear out" the distributions of the measured data.

The choice of model GM strength seems an unlikely explanation for the data/model differences: Indeed, an identical MCPE simulation with a GM strength near 4.6 (not shown here) did not predict a SI as large as that observed for path ID-3—while the same simulation overpredicts the SI for paths ID+4 and ID-4 by about a factor of three.

Ray tracing through the background sound-speed profile indicated that acoustic paths with a shallow UTP near 60 m would turn below the average mixed-layer depth seen in the 19 CTD casts. The vertical Fresnel zone around that shallow-turning ray, however, extends vertically from 10 to 100 m depth at the upper turning point—allowing for the possibility that this acoustic path interacted with the mixed layer. This may introduce a long-time-scale (diurnal) modulation that is not part of a standard GM internal-wave model. No attempt was made to include a mixed layer in the MCPE model as the primary processes that drive the mixed-layer depth (Soloviev and Lukas, 2006) are not encompassed by the GM model.

An observation that could be related to the deep fades is that the three or four shallowest microCATs on the DVLA (shown in Fig. 6) showed an increase in sound speed near YD 110, followed by a decrease, and then a period of very little fluctuation from YD 112 to YD 122 or 123—despite large variability measured by the deeper sensors during that same period of time. These features coincide with the westward motion past the DVLA of the warm mesoscale feature, visible just to the southwest of it in Fig. 1 (the westward motion is apparent from additional SSH maps from AVISO at 7-days intervals but that are not shown here). This lack of sound-speed fluctuations in the upper ocean from YD 112 to YD 122 would seem to indicate that the water at those depths was well-mixed or at least that the vertical gradient of sound speed was diminished during that period of time. The changing positions of mesoscale features may be related to this apparent change in the amount of vertical displacement observed by those shallowest sensors.

Simulations of a random eddy field with an assumed spectrum have been performed by Freitas (2008) and indicate that the presence of eddies can have a significant impact on acoustic propagation; in particular, she concluded that the eddy field caused acoustic energy to become trapped in surface ducts, caused shifts in horizontal and vertical convergence zone position, and caused convergence zone spreading. It is apparent from the temperature measurements shown in Fig. 5 that there is a strong large-scale range dependence to the sound speed profile. It is difficult to say from the work presented here whether the presence of mesoscale eddies has had an effect on the intensity. The good data-model agreement for arrivals with UTP between 260 and 451 m would suggest that the effect was not significant for those paths—but the cause of the deep fades in path ID-3 requires further study.

Peaks at tidal frequencies are prominent in the spectrum of sound speed variability measured by the CTD sensors on the DVLA. Further evidence of the time dependence of the large-scale sound-speed field appears in the XBT transects shown in Fig. 5. Some transects overlapped in latitude, for example near 21.6° N, and a decrease in temperature is apparent—though the time elapsed between the transects does not allow one to infer much about the time scale of that variability.

An important feature of the observed deep fades is the time dependence. Two and possibly part of a third deep fade are visible in the 1550 m time series shown in the bottom panel of Fig. 4. The intensity appears, roughly, to have a 5 dB fade during year day 117, a 10 dB fade during year day 118, and another 10 dB fade during year day 119. The character of these fades is not sinusoidal, making it difficult to identify a particular periodicity, especially given only two clearly recognizable 10 dB fading events. It seems possible that the time scale is related to the observed strong local internal tides (Colosi et al., 2013).

The MCPE modeling presented in this report has made the assumption that the GM spectrum is an accurate representation of sound-speed fluctuations in the Philippine Sea. It is possible that the model-data discrepancy for paths turning in the extreme upper ocean is due to disagreement with the GM spectrum there, but the similarity to tidal time scales of the deep fades would seem to at least partially implicate the local internal tides.

Construction of a model or models that address the mesoscale variability and/or internal tides go beyond the MCPE approach taken here, however, which has made the assumption of a range-independent background sound-speed profile. Attempts to include range dependence in MCPE models are not unheard of; Wolfson and Spiesberger (1999) included a range-dependent background, for example, in a study of a long-range experiment.

3356   J. Acoust. Soc. Am., Vol. 134, No. 4, Pt. 2, October 2013

10

White et al.: Intensity stats 284-Hz transmission to 107 km

VI. CONCLUSIONS

Despite the simplification of range-independence and the exclusion of internal tides from MCPE model simulations, the predictions of the SI, σ_i^2, and the distribution of $I/\langle I \rangle$ for paths with UTPs below the extreme upper ocean generally agree with observations—the only model adjustment made was of the GM strength. This conclusion is in agreement with the results presented in Colosi *et al.* (2013) (to the extent that the MCPE model provides a validation of the ocean model), who studied the PhilSea09 environmental measurements more extensively. Their results were consistent with the GM spectral model's assumptions of horizontal isotropy and homogeneity (for diffuse internal waves), and they conclude that the GM spectrum could be used as an input to acoustic fluctuation calculations. The measures of intensity fluctuations studied here, the SI and σ_i^2, did not appear to be strongly influenced by the number of UTPs in the path—although a compensating effect due to differences in UTP depth cannot be ruled out. Some of the differences between the distributions of the simulated and measured intensities may be due to the shorter duration of the measured time series; an experiment with a longer duration would be required to resolve the ambiguity. Enhanced variability in the form of long-period deep fades is observed for paths turning in the extreme upper ocean; this enhanced variability is not predicted by the MCPE model employed here and will be the subject of a follow-on report.

ACKNOWLEDGMENTS

APPENDIX: PE MODEL AND CONVERGENCE TESTS

The NSPE was chosen because it provides test cases and is actively maintained by the U.S. Navy. The code includes an implementation of a split-step Fourier (Tappert, 1977) algorithm, and an implementation of a split-step Padé algorithm derived from the range-dependent acoustic model (RAM; Collins, 1993). We used the split-step Padé version. The NSPE is capable of propagation through a range-dependent sound-speed field such as that of an internal-wave perturbed ocean model environment. The angle between the horizontal and the direction of acoustic paths leaving the source was well within the limits for this PE.

Convergence tests were performed on the number of modes used in the internal wave simulator and on the range-step taken in the PE code. Features in the sound speed field that are much smaller than the acoustic wavelength will have a negligible effect on the propagation of acoustic waves; see e.g., Hegewisch *et al.* (2005). The criterion used to determine convergence was the normalized sum of squared errors

$$e_m = \frac{\sum_{i=1}^{n} (p_{m+10}(t_i) - p_m(t_i))^2}{\sum_{i=1}^{n} (p_m(t_i))^2}, \qquad \text{(A1)}$$

where $p(t_i)$ is the n-point real pressure time series computed by propagation of a broadband acoustic signal through a single instance of a GM internal wave perturbed random ocean composed of m modes. This measure of convergence fell to a value of $10 \log_{10}(e_m) = -30$, or 0.1%, when 200 vertical internal wave modes were included in the random ocean. A similar metric was used to determine convergence for range-step except that the range-step was halved each time. A value of -30 was reached when the range step was 25 m.

Ten Padé coefficients were retained to avoid performing an additional convergence test on the number of coefficients.

Alford, M. H., MacKinnon, J. A., Nash, J. D., Simmons, H., Pickering, A., Klymak, J. M., Pinkel, R., Sun, O., Rainville, L., Musgrave, R., Beitzel, T., Fu, K., and Lu, C. (**2011**). "Energy flux and dissipation in Luzon Strait: Two tales of two ridges," J. Phys. Oceanogr. **41**, 2211–2222.

Andrew, R. K. (**2009**). "The APL/UW multiport acoustic projector system," Technical Report APL/UW TR-0902 (Applied Physics Laboratory, University of Washington, Seattle, WA).

Aviso and support from Cnes (**2012**). "Ssalto and Duacs products," http://www.aviso.oceanobs.com/duacs (Last viewed March 24, 2012).

Birdsall, T. G. (**1995**). "Signals and signal processing for acoustic monitoring of ocean processes," in *1995 International Conf. on Acoustics, Speech, and Signal Processing* (IEEE, Detroit, MI), pp. 2767–2770.

Birdsall, T. G., and Metzger, K. (**1986**). "Factor inverse matched filtering," J. Acoust. Soc. Am. **79**, 91–99.

Bowlin, J. B., Spiesberger, J. L., Duda, T. F., and Freitag, L. F. (**1992**). "Ocean acoustical ray-tracing software ray," Technical Report WHOI-93-10 (Woods Hole Oceanographic Institution, Woods Hole, MA).

Cojbasic, V., and Tomovic, A. (**2007**). "Nonparametric confidence intervals for population variance of one sample and the difference of variances of two samples," Comp. Stat. Data Anal. **51**, 5562–5578.

Collins, M. D. (**1993**). "A split-step padé solution for the parabolic equation method," J. Acoust. Soc. Am. **93**, 1736–1742.

Colosi, J. A., Flatté, S. M., and Bracher, C. (**1994**). "Internal wave effects on 1000 km oceanic acoustic pulse propagation: Simulation and comparison with experiment," J. Acoust. Soc. Am. **96**, 452–468.

Colosi, J. A., van Uffelen, L. J., Cornuelle, B. D., Dzieciuch, M. A., Worcester, P. F., Dushaw, B. D., and Ramp, S. R. (**2013**). "Observations of sound-speed fluctuations in the western Philippine Sea in the spring of 2009," J. Acoust. Soc. Am. **134**, 3185–3200.

Colosi, J. A., Xu, J., Worcester, P. F., Dzieciuch, M. A., Howe, B. M., and Mercer, J. A. (**2009**). "Temporal and vertical scales of acoustic fluctuations for 75-Hz, broadband transmissions to 87-km range in the eastern North Pacific Ocean," J. Acoust. Soc. Am. **126**, 1069–1083.

Davison, A. C., and Hinkley, D. V. (**1997**). *Bootstrap Methods and Their Applications (Cambridge Series in Statistical and Probabilistic Mathematics)* (Cambridge University Press, Cambridge UK), Chap. 8, pp. 385–436.

Dushaw, B. D., Howe, B. M., Mercer, J. A., and Spindel, R. C. (**1999**). "Multi-megameter-range acoustic data obtained by bottom-mounted hydrophone arrays for measurement of ocean temperature," J. Ocean. Eng. **24**, 202–214.

Ewart, T. E. (**1976**). "Acoustic fluctuations in the open ocean—a measurement using a fixed refracted path," J. Acoust. Soc. Am. **60**, 46–59.

Ewart, T. E., and Reynolds, S. A. (**1984**). "The mid-ocean acoustic transmission experiment, MATE," J. Acoust. Soc. Am. **75**, 785–802.

Flatté, S. M., Dashen, R., Munk, W. H., Watson, K., and Zachariasen, F. (**1979**). *Sound Transmission through a Fluctuating Ocean* (Cambridge University Press, Cambridge, UK).

Freitas, K. M. (**2008**). "Improving accuracy of acoustic prediction in the Philippine Sea through incorporation of mesoscale environmental effects," Master's thesis, Naval Postgraduate School, Monterey, CA.

J. Acoust. Soc. Am., Vol. 134, No. 4, Pt. 2, October 2013   White *et al.*: Intensity stats 284-Hz transmission to 107 km   3357

11

Hegewisch, K. C., Cerruti, N. R., and Tomsovic, S. (**2005**). "Ocean acoustic wave propagation and ray method correspondence: Internal wave fine structure," J. Acoust. Soc. Am. **117**, 1582–1594.

Henyey, F. S., and Reynolds, S. A. (**2013**). "A numerical simulator of ocean internal waves for long-range acoustics," Technical Report APL-UW TM 1-13 (Applied Physics Laboratory, University of Washington, Seattle, WA).

Kobashi, F., and Kawamura, H. (**2001**). "Variation of sea surface height at periods of 65-220 days in the subtropical gyre of the North Pacific," J. Geophys. Res. **106**, doi: 10.1029%2F2000JC000361, 26817–26831.

Levine, M. D. (**2002**). "A modification of the Garrett–Munk internal wave spectrum," J. Phys. Oceanogr. **32**, 3166–3181.

Mercer, J. A., Colosi, J. A., Howe, B. M., Dzieciuch, M. A., Stephen, R., and Worcester, P. F. (**2009**). "LOAPEX: The long-range ocean acoustic propagation experiment," J. Ocean. Eng. **34**, 1–11.

Munk, W. H. (**1981**). "Internal waves and small-scale processes," in *The Evolution of Physical Oceanography*, edited by C. Wunsch and B. Warren (MIT Press, Cambridge, MA), pp. 264–291.

Munk, W. H., Worcester, P. F., and Wunsch, C. (**1995**). *Ocean Acoustic Tomography* (Cambridge University Press, Cambridge, UK), pp. 190–195.

Pinkel, R. (**1984**). "Doppler sonar observations of internal waves: The wavenumber-frequency spectrum," J. Phys. Oceanogr. **14**, 1249–1270.

Reynolds, S. A., Flatté, S. M., Dashen, R., Buehler, B., and Maciejewski, P. (**1985**). "AFAR measurements of acoustic mutual coherence functions of time and frequency," J. Acoust. Soc. Am. **77**, 1723–1731.

Soloviev, A., and Lukas, R. (**2006**). *The Near-Surface Layer of the Ocean, Structure, Dynamics and Applications* (Springer, The Netherlands), Chap. 1, p. 63.

Tappert, F. D. (**1977**). "The parabolic approximation method," in *Lecture Notes in Physics No.70*, edited by J. B. Keller and J. S. Papadakis (Springer-Verlag, New York), pp. 224–287.

TEOS-10 (**2010**). "Thermodynamic equation of state - 2010," http://wwwos-10.org (Last viewed March 24, 2012).

van Uffelen, L. J. (**2009**). "Acoustic shadow-zone arrivals at long range in the North Pacific Ocean," Ph.D. thesis, University of California, San Diego CA.

van Uffelen, L. J., Worcester, P. F., Dzieciuch, M. A., Rudnick, D. L., and Colosi, J. A. (**2010**). "Effects of upper ocean sound-speed structure on deep acoustic shadow-zone arrivals at 500- and 1000-km range," J. Acoust. Soc. Am. **127**, 2169–2181.

Wolfson, M. A., and Spiesberger, J. L. (**1999**). "Full-wave simulation of the forward scattering of sound in a structured ocean: A comparison with observations," J. Acoust. Soc. Am. **106**, 1293–1306.

Worcester, P. F. (**1979**). "Reciprocal acoustic transmission in a midocean environment: Fluctuations," J. Acoust. Soc. Am. **66**, 1173–1181.

Worcester, P. F., Andrew, R. K., Baggeroer, A. B., Colosi, J. A., D'Spain, G. L., Dzieciuch, M. A., Heaney, K. D., Howe, B. M., Kemp, J. N., Mercer, J. A., Stephen, R. A., and van Uffelen, L. J. (**2012**). "The North Pacific Acoustic Laboratory (NPAL) deep-water acoustic propagation experiments in the Philippine Sea," J. Acoust. Soc. Am. **131**, 3352(A).

Worcester, P. F., Carey, S., Dzieciuch, M. A., Green, L. L., Horwitt, D., Lemire, J. C., and Norenberg, M. (**2009**). "Distributed vertical line array (DVLA) acoustic receiver," in *Proceedings of the 3rd International Conf. on Underwater Acoustic Measurements*, edited by J. S. Papadakis and L. Bjørnø (Foundation for Research and Technology Hellas, Nafplion, Greece), pp. 113–118.

Worcester, P. F., Cornuelle, B. D., Dzieciuch, M. A., Munk, W. H., Howe, B. M., Mercer, J. A., Spindel, R. C., Colosi, J. A., Metzger, K., Birdsall, T. G., and Baggeroer, A. B. (**1999**). "A test of basin-scale acoustic thermometry using a large-aperture vertical array at 3250-km range in the eastern North Pacific Ocean," J. Acoust. Soc. Am. **105**, 3185–3201.

Worcester, P. F., and Spindel, R. C. (**2005**). "North Pacific Acoustic Laboratory," J. Acoust. Soc. Am. **117**, 1499–1510.

Xu, J. (**2007**). "Effects of internal waves on low frequency, long range, acoustic propagation in the deep ocean," Ph.D. thesis, Massachusetts Institute of Technology, Cambridge, MA.

12

CRUISES AND AT-SEA EXPERIENCE	**ATOC Source-recovery cruise, #1**, off the California coast	**June 2008**
	PhilSea09 Experiment, Philippine Sea	**April – May 2009**
	PhilSea10 Experiment, Philippine Sea	**May 2010**
	ATOC Source-recovery cruise, #2, off the California coast	**July 2011**

PUBLICATIONS

Andrew W. White, Rex K. Andrew, James A. Mercer, Peter F. Worcester, Matthew A. Dzieciuch, and John A. Colosi, "Wavefront intensity statistics for 284-Hz broadband transmissions to 107-km range in the Philippine Sea: observations and modeling", *J. Acoust. Soc. Am.*, **134**(4), Pt. 2, October 2013

Andrew W. White, "Underwater Acoustic Propagation in the Philippine Sea: Intensity Fluctuations", University of Washington, PhD thesis, 2013

CONFERENCE PRESENTATIONS

Andrew W. White, Rex K. Andrew, James A. Mercer, Peter F. Worcester, Matthew A. Dzieciuch, John A. Colosi, Lora J. Van Uffelen, and and Bruce M. Howe "Deep fades in intensity: Exploration of measurement-Monte Carlo parabolic equation mismatch in the Philippine Sea", *J. Acoust. Soc. Am.*, **134**, 4001 (2013)

Andrew W. White, Rex K. Andrew, James A. Mercer, Peter F. Worcester, and Matthew A. Dzieciuch, "Intensity statistics for low-frequency acoustic transmissions in the Philippine Sea", 2013 Joint Undersea Warfare Technology Fall Conference

Andrew W. White, Rex K. Andrew, James A. Mercer, Peter F. Worcester, and Matthew A. Dzieciuch, "Measured low-frequency intensity fluctuations over a 107 km path in the 2009-2010 Philippine Sea Experiment", *J. Acoust. Soc. Am.*, **131**(4), April 2012

Rex K. Andrew, Andrew W. White, James Mercer, Peter Worcester, Matthew Dzieciuch, and John Colosi, "Theoretical fluctuation predictions for low-frequency acoustical propagation ranges of 25 to 107 km in the 2009-2010 Philippine Sea experiment", *J. Acoust. Soc. Am.*, **131**(4), April 2012

James Mercer, Rex Andrew, Linda Buck, Gerald D'Spain, Matthew Dzieciuch, Andy Ganse, Frank Henyey, Andrew White, and Peter Worcester, "The 2009 Philippine Sea Pilot Study/Engineering Test and the 2010 Philippine Sea Experiment: University of Washington cruises", *J. Acoust. Soc. Am.,* **131**(4), April 2012

Andrew W. White, Rex K. Andrew, James A. Mercer, Frank S. Henyey, "Low-frequency broadband acoustic signal characteristics in the Philippine Sea", 2011 NPAL Workshop, Washington DC

Andrew W. White, Frank S. Henyey, Rex K. Andrew, James A. Mercer, "Predictions of fluctuation statistics of a broad-band acoustic signal in the Philippine Sea '09 environment by Monte Carlo PE", 2010 NPAL Workshop, Carmel, California

James Mercer, Rex Andrew, Andy Ganse, Andrew White, and Gerald DSpain, "The University of Washingtons Applied Physics Laboratorys participation in the Philippine Sea 2009 and Philippine Sea 2010 experiments: A summary.", *J. Acoust. Soc. Am.*, **128**(4), October 2010

Andrew W. White, Frank S. Henyey, Rex K. Andrew, James A. Mercer, Peter F. Worcester, and Matthew A. Dzieciuch, "Comparison of fluctuations of a broad-band pulsed acoustic signal in the Philippine Sea to simulation", *J. Acoust. Soc. Am.*, **126**(4), October 2009

Andrew W. White, Frank S. Henyey, Rex K. Andrew, James A. Mercer, Peter F. Worcester, and Matthew A. Dzieciuch, "Preliminary analysis of PhilSea09 CTD and XBT casts", 2009 NPAL Workshop, Anza Borrego, California

REPORT DOCUMENTATION PAGE

Form Approved
OMB No. 0704-0188

1. REPORT DATE *(DD-MM-YYYY)*	2. REPORT TYPE	3. DATES COVERED *(From - To)*
17-03-2014	Final Technical Report	01 Jan 2008 - 31 Dec 2013

4. TITLE AND SUBTITLE

Deep-Water Acoustics [Special Graduate Traineeship in Ocean Acoustics]

5a. CONTRACT NUMBER

5b. GRANT NUMBER
N00014-08-1-0200

5c. PROGRAM ELEMENT NUMBER

6. AUTHOR(S)
Andrew W. White
Rex K. Andrew
James A. Mercer
Peter F. Worcester
Matthew A. Dzieciuch
John A. Colosi

5d. PROJECT NUMBER

5e. TASK NUMBER

5f. WORK UNIT NUMBER

7. PERFORMING ORGANIZATION NAME(S) AND ADDRESS(ES)

Applied Physics Laboratory
University of Washington
1014 NE 40th St.
Seattle, WA 98105

8. PERFORMING ORGANIZATION REPORT NUMBER

9. SPONSORING/MONITORING AGENCY NAME(S) AND ADDRESS(ES)

Dr. Robert Headrick, Code 322
Office of Naval Research
875 North Randolph Street
Arlington, VA 22203

10. SPONSOR/MONITOR'S ACRONYM(S)
ONR

11. SPONSOR/MONITOR'S REPORT NUMBER(S)

12. DISTRIBUTION/AVAILABILITY STATEMENT

DISTRIBUTION STATEMENT A: Approved for public release, distribution unlimited.

13. SUPPLEMENTARY NOTES

14. ABSTRACT

In the spring of 2009, broadband transmissions from a ship-suspended source with a 284-Hz center frequency were received on a moored and navigated vertical array of hydrophones over a range of 107 km in the Philippine Sea. During a 60-h period over 19 000 transmissions were carried out. The observed wavefront arrival structure reveals four distinct purely refracted acoustic paths: One with a single upper turning point near 80m depth, two with a pair of upper turning points at a depth of roughly 300 m, and one with three upper turning points at 420 m. Individual path intensity, defined as the absolute square of the center frequency Fourier component for that arrival, was estimated over the 60-h duration and used to compute scintillation index and log-intensity variance. Monte Carlo parabolic equation simulations using internal-wave induced sound speed perturbations obeying the Garrett–Munk internal-wave energy spectrum were in agreement with measured data for the three deeper-turning paths but differed by as much as a factor of four for the near surface-interacting path$\bullet$ 1ln(1= h). The approach toward equilibrium, as me$\cdots$ by the scintillation index, is exponential: $i2(t)$ 12 exp($\bullet \bullet$ t)ln(1= h) +1 + O(h=t2). This provides a

15. SUBJECT TERMS

vertical array, scintillation index, log-intensity variance, Monte Carlo parabolic equation simulations, Garrett - Munk internal-wave energy spectrum

16. SECURITY CLASSIFICATION OF:			17. LIMITATION OF ABSTRACT	18. NUMBER OF PAGES	19a. NAME OF RESPONSIBLE PERSON
a. REPORT	b. ABSTRACT	c. THIS PAGE			James A. Mercer
U	U	U	U	14	19b. TELEPHONE NUMBER *(Include area code)* (206) 543-1300

Reset

Standard Form 298 (Rev. 8/98)
Prescribed by ANSI Std. Z39.18